



Brief communication: Unravelling the composition and microstructure of a permafrost core using X-ray computed tomography

Jan Nitzbon¹, Damir Gadylyaev^{1,3}, Steffen Schlüter², John Maximilian Köhne², Guido Grosse^{1,3}, and Julia Boike^{1,4}

¹Permafrost Research Section, Alfred Wegener Institute Helmholtz Centre for Polar and Marine Research, Potsdam, Germany

²Department of Soil System Science, Helmholtz Centre for Environmental Research – UFZ, Halle (Saale), Germany

³Institute of Geosciences, University of Potsdam, Potsdam, Germany

⁴Geography Department, Humboldt-Universität zu Berlin, Berlin, Germany

Correspondence: Jan Nitzbon (jan.nitzbon@awi.de)

Abstract. The microstructure of permafrost ground contains clues to its formation and hence its preconditioning to future change. We applied X-ray computed microtomography (CT) to obtain high-resolution data ($\Delta x = 50 \mu\text{m}$) of the composition of a 164 cm long permafrost core drilled in a Yedoma upland in northeastern Siberia. The CT analysis allowed to directly map and quantify excess ice, gas inclusions, and two distinct sediment phases. Using laboratory measurements of coarsely-resolved core samples, we statistically estimated the composition of the sediment phases and indirectly quantified pore ice, organic, and mineral contents. We conclude that CT is a promising method for obtaining physical properties of permafrost cores which opens novel research potentials.

1 Introduction

Arctic permafrost ground contains considerable amounts ground ice and organic matter. Melting of excess ice – ground ice which exceeds the volume of the sediment’s pore space – leads to ground subsidence, thermokarst formation, thereby affecting Arctic ecosystems (Kokelj and Jorgenson, 2013) and posing a risk for infrastructure failure (Schneider von Deimling et al., 2021). Thawing and subsequent decomposition of organic matter can increase greenhouse gas release in Arctic lowlands, potentially causing a positive climate feedback (Schuur et al., 2015). Hence, an accurate quantification of the amounts and the distribution of both ground ice and organic matter in permafrost ground is needed in various realms of permafrost research, for example, to improve carbon stock assessments (Strauss et al., 2017) and model projections of permafrost thaw (Nitzbon et al., 2020). In addition to excess ice and organic matter, also the structure and contents of other permafrost constituents such as pore ice, gas inclusions, and mineral grains are of interest, as they affect material properties and provide additional insights into the processes that formed the soil. Permafrost composition and the cryostructure at a given site typically are characterized by visual description of exposures or drill cores from a given site (e.g., Kanevskiy et al. (2011)). A quantitative determination of the composition of permafrost is then approached by sub-sampling exposures or cores along the direction of deposition, and then measuring ground ice, organic carbon, and mineral contents through laboratory analyses of the samples (e.g., Schirrmeister



et al. (2011)). However, this approach is destructive, has a low stratigraphic resolution on the order of 1 to 5 cm for cores, and does not provide information on the spatial configuration of the samples' constituents. Furthermore, measuring gas contents and distinguishing excess ice from pore ice are very inaccurate using those classical analysis techniques.

25 In recent years, microstructure analysis with X-ray CT has turned into a standard method in various geoscience disciplines like soil science, stratigraphy, or glaciology (Cnudde and Boone, 2013; Withers et al., 2021; Oggier and Eicken, 2022). Across disciplines, the general aim of non-invasive imaging like CT is to deduce functional behavior or process understanding at larger scales through mapping of the microscale composition and morphology of all constituents in a sample Cnudde and Boone (2013). Despite the broad potential for applications which require in-depth knowledge of the composition and physical
30 properties of permafrost, there are only few reports of CT being applied to study frozen soil samples (Torrance et al., 2008). Calmels and Allard (2004) pioneered the use of CT to measure excess ice and gas contents in ice-rich permafrost of a lithalsa landform. Calmels and Allard (2008) built on this and used CT scans to establish links between various permafrost landforms and microscale cryostructures. CT scans have further been used to study ground ice structures and periglacial processes in Arctic (Calmels et al., 2008, 2012) and Antarctic (Lapalme et al., 2017) permafrost. More recently, Romanenko et al. (2017)
35 and Rooney et al. (2022) used CT imaging to investigate dynamic changes in the pore space due to freezing and thawing.

However, we are not aware of any studies that aimed at a detailed quantification of the constituents of permafrost drill cores, in particular including a distinction between all major constituents of permafrost soils as a porous composite material: excess ice, pore ice, organic matter, mineral grains, and gas inclusions. Moreover, a systematic quantitative comparison between the laboratory-measured and the CT-derived composition of permafrost cores has not been done to date.

40 In the present study, we use CT imaging to investigate a permafrost drill core from a Yedoma upland in northeast Siberia. Specifically, we assess the suitability of CT imaging and image processing methods to quantify vertical profiles of the volumetric contents as well as the structures of gas, excess ice, pore ice, organic matter, and mineral constituents. We further use laboratory measurements of total ice, organic, and mineral contents to evaluate and complement the CT analysis with the overall goal to obtain a detailed high-resolution (50 μm) three-dimensional composition of the entire permafrost core. With our
45 work we propose a methodological advancement in employing CT imaging for the measurement of volumetric contents and structures of all major constituents of permafrost as a porous composite material, which opens potential further research on microstructure and physical properties.

2 Methods

2.1 Field site and coring

50 The permafrost core analyzed in this work was sampled from an ice-rich Yedoma permafrost upland plateau on Kurunghakh Island, Lena River Delta, northeast Siberia (72.36613 N, 126.27272 E). Kurunghakh Island is the easternmost portion of the structurally elevated western Lena River Delta and rises up to 55 m above sea level. The core was mechanically drilled during the field campaign in September 2017. A soil pit was excavated to the maximum thaw depth of 20 cm followed by drilling and coring of the frozen material underneath to a depth of 164 cm. The diameter of the frozen core was 7.5 cm. The frozen core



55 pieces were wrapped and labeled individually at the field site and stored in the freezers at the Samoylov research station. The core samples were shipped in frozen condition to AWI Potsdam's laboratory during fall 2017. The samples were kept frozen until further analysis.

2.2 CT analysis of the entire core

2.2.1 Scanning

60 The permafrost core was scanned in February 2019 at the Helmholtz Center for Environmental Research. First, the permafrost core was assembled in various up to about 30 cm long segments each of which fit into the X-ray CT chamber. The cores were kept frozen until image acquisition and shielded with bubble wrap during the acquisition. The segments were then scanned using an X-ray microtomography system (Nikon Metrology, XT H 225) with settings adjusted to 150 kV, 320 μ A, 500 ms exposure time and a 0.5 mm copper filter for beam hardening reduction. 2748 projections were acquired during a full rotation,
65 with 1 frame per projection. The core segments were scanned in two vertical steps (top, bottom) with sufficient overlap to put the two tomograms together afterwards. The total scan time for one segment amounted to about 23 minutes during which melting was negligible. Finally, the radiographs were reconstructed into a 3D tomogram with a voxel size of 50 μ m and 8-bit grayscale resolution using the CT Pro 3D software by Nikon Metrology. The grayscale range of each CT scan was normalized by setting the darkest and brightest 0.2 percentile to 0 and 255 respectively.

70 2.2.2 Image preprocessing

Image preprocessing (along with image analysis and segmentation) was applied to the whole core length of 164 cm and consisted of four steps, all of which were done using ImageJ/FIJI (Schindelin et al., 2012). First, cylindrical regions of interest (ROI) were determined for each segment, which were fully inscribed in the core without extending beyond its uneven boundaries. Second, depth intervals with artifacts, e.g. due to cracks in the core, were identified visually in order to exclude them
75 from quantitative analysis. Third overlaps between adjacent scans were removed manually by identifying identical horizontal slices in both images. Lastly, image noise was removed by applying three consecutive 2D Non-Local Means filtering steps, one in each principal direction. The filter settings (noise standard deviation = 6, smoothing factor = 1) were adjusted to the noise level in the raw images, which resulted from the relatively short scan time to reduce melting in the X-ray CT chamber.

2.2.3 Image segmentation

80 Visual inspection of the data indicated that the cores contained four material classes, which could clearly be separated by their distinct peaks in the histogram. These were (from dark to bright) gas-filled pores, excess ice and two mixed sediment phases of unknown composition denoted as phases A and B. Manual threshold detection with adjustments for different illumination and different numbers of material classes in individual segments resulted in robust segmentation results which was checked by visual inspection (Fig. 1).



85 2.3 Laboratory analysis of core samples

In August 2020, the frozen core was prepared for further lab analysis in the cold laboratory (below 0°C temperature). First, all samples were photographed and visually described. Then, the core was cut in into smaller sections. All surfaces and saw blades were cleaned with ethanol before and during the cutting. A total of $N_j = 66$ sub samples was obtained with a thickness ranging between 0.9 cm to 1.9 cm, each associated with a central depth z_j . The volume V_j and weight $m_{\text{wet},j}$ of all frozen sub samples were measured. The samples were then allowed to thaw and then dried in an oven at a temperature of 100°C for 24 hours. The total ice loss was then determined by subtracting the dry weight from the wet weight of the sample: $m_i = m_{\text{wet}} - m_{\text{dry}}$. Then, the volumetric total ice content was calculated as

$$\theta_i(z_j) = m_{i,j}/(\rho_i V_j) \quad , \quad (1)$$

with $\rho_i = 916 \text{ kg m}^{-3}$ being the density of ice.

95 The remaining dried sediment samples (grain size fraction < 2 mm) were homogenized and analysed for the total organic carbon (TOC) content using standard laboratory procedures. The grain size fraction > 2 mm was zero, which is characteristic for predominantly silty material of the Yedoma complex. The gravimetric TOC content (g_{TOC}) was measured twice with a Vario Max C analyzer after carbonate was removed by adding hydrochloric acid (4%). For a valid comparison between the laboratory and CT data, we converted the TOC contents into contents of (intact) organic matter. For this, the TOC contents were multiplied with the adapted van Bemmelen Factor of $f_{\text{vB}} = 2$ suggested by Pribyl (2010). The volumetric organic matter content ($\theta_o(z_j)$) was then calculated for each sample $j = 1 \dots N_j$ as:

$$\theta_o(z_j) = (f_{\text{vB}} g_{\text{TOC},j}) m_{\text{dry},j}/(\rho_o V_j) \quad , \quad (2)$$

where we assumed a density of organic matter of $\rho_o = 1300 \text{ kg m}^{-3}$ (Adams, 1973).

The mineral weight was determined by subtracting the organic matter weight from the total weight of the dried sample 105 ($m_m = (1 - f_{\text{vB}} g_{\text{TOC}}) m_{\text{dry}}$). The volumetric mineral content ($\theta_m(z_j)$) was then calculated for each sample $j = 1 \dots N_j$ as:

$$\theta_m(z_j) = m_{m,j}/(\rho_m V_j) \quad , \quad (3)$$

where we used the densities of quartz for the mineral sediment ($\rho_m = 2650 \text{ kg m}^{-3}$).

2.4 Estimating the composition of the sediment phases

Since the CT images do not allow to estimate the composition of the sediment phases directly, we used the volumetric total ice 110 (θ_i), mineral (θ_m), and organic (θ_o) contents that were determined in the lab (Sec. 2.3) to infer their composition statistically. For this, we assumed them to be saturated and thus composed of organic matter ($\gamma_{A/B,o} \in [0, 1]$), mineral grains ($\gamma_{A/B,m} \in [0, 1]$) and pore ice ($\gamma_{A/B,i} \in [0, 1]$):

$$\gamma_{A,\text{pi}} + \gamma_{A,o} + \gamma_{A,m} = 1$$

$$\gamma_{B,\text{pi}} + \gamma_{B,o} + \gamma_{B,m} = 1 \quad (4)$$



115 Note that the pore ice fractions $\gamma_{A/B,pi}$ correspond to the porosity of the respective sediment phase under the assumption of saturated sediment. For each of the $j = 1 \dots N_j$ samples the following linear equation system can be formulated:

$$\begin{aligned}\theta_o(z_j) &= \gamma_{A,o} \theta_A(z_j) + \gamma_{B,o} \theta_B(z_j) \\ \theta_m(z_j) &= \gamma_{A,m} \theta_A(z_j) + \gamma_{B,m} \theta_B(z_j) \\ \theta_i(z_j) &= \underbrace{(1 - \gamma_{A,m} - \gamma_{A,o}) \theta_A(z_j) + (1 - \gamma_{B,m} - \gamma_{B,o}) \theta_B(z_j)}_{\theta_{pi}(z_j)} + \theta_{ei}(z_j)\end{aligned}\quad (5)$$

120 where Eq. (4) was used to express the pore ice fraction of phases A and B in terms of their respective organic and mineral fractions. For this over-determined system of equations we performed a linear least-squares regression using the scikit-learn Python package (https://scikit-learn.org/stable/modules/generated/sklearn.linear_model.LinearRegression.html) to find the best-fitting parameters $\hat{\gamma}_{A/B,m/o}$. For the left hand side of equation system (5) we took as input the laboratory estimates of the mineral, organic matter and total ice contents ($\theta_{m/o/i}(z_j)$). For the right hand side we took as input the estimates of the volumetric fractions
125 of the sediment phases A,B and the excess ice phase from the CT analysis ($\theta_{A/B/ei}(z_j)$), averaged over the same depth-intervals as the laboratory samples.

Finally, we used the fitted parameters ($\hat{\gamma}_{A/B,m/o/pi}$) and the high-resolution profiles from the CT analysis ($\theta_{A/B/ei/a}(z)$) as input to the equations (5) to determine a high-resolution profile for the organic ($\theta_o(z)$), mineral ($\theta_m(z)$), and total ice contents ($\theta_i(z)$) of the entire core.

130 3 Results

3.1 General composition and cryostructures

Figure 1 provides an overview of the entire core after drilling (a), CT scanning (b), and image segmentation (c,d). The **photography** of the core (Fig. 1 a) allowed us to distinguish two major compartments: the first ranges from about 20 cm to 85 cm depth and contains sediment with ice inclusions; the second extends from about 85 cm depth to the end of the core and is essentially
135 composed of excess ice.

The CT image of the core (b) allowed us to identify characteristic cryostructures such as segregated ice lenses (e.g., Fig. 1 e) and reticulate ice (e.g., **between 30 cm and 40 cm depth**) in the sedimentary upper part of the core. In the lower part, we identified small inclusions of gas ("bubbles") of circular or vertically elongated shape within the excess ice (Fig. 1 h).

The image segmented into gas, excess ice, and **sedimentary phases** (Fig. 1 c) suggested a further subdivision of the sedimentary compartment into an excess ice-rich upper part from 20 cm to about 60 cm (Fig. 1 f), and a sediment-rich part between
140 60 cm and 85 cm depth (Fig. 1 g). **Hence, we subsequently distinguish three major parts of the core: the core section between 20 cm and 60 cm depth as the upper part; the section between 60 cm and 85 cm as the middle part; and the section below 85 cm depth as the lower part.**

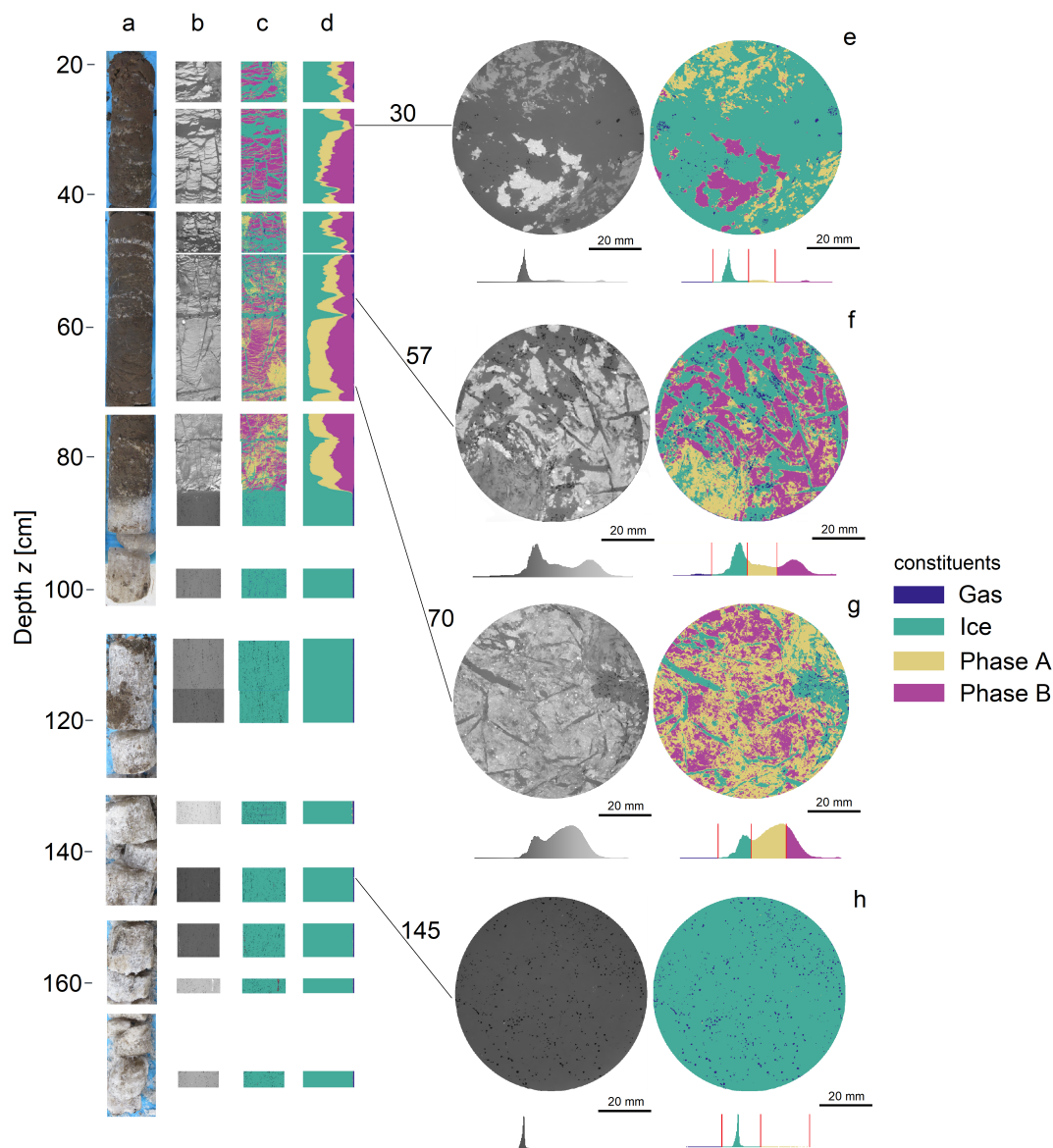


Figure 1. Overview of the studied permafrost core (a-d). Photography taken after drilling (a); absorption images from CT scanner after preprocessing (b) and after segmentation (c); volumetric composition in terms of gas, excess ice, phase A, and phase B (d). The right part (e-h) shows exemplary horizontal slices of the preprocessed and segmented CT images, as well as the histograms of brightness values.

3.2 Direct estimation of gas and excess ice contents

145 From the segmented CT images, we directly obtained vertical profiles of volumetric gas ($\theta_a(z)$, Figure 2 a) and excess ice ($\theta_{ei}(z)$, Figure 2 b) contents. As a general pattern, we found that gas contents are positively correlated with excess ice contents

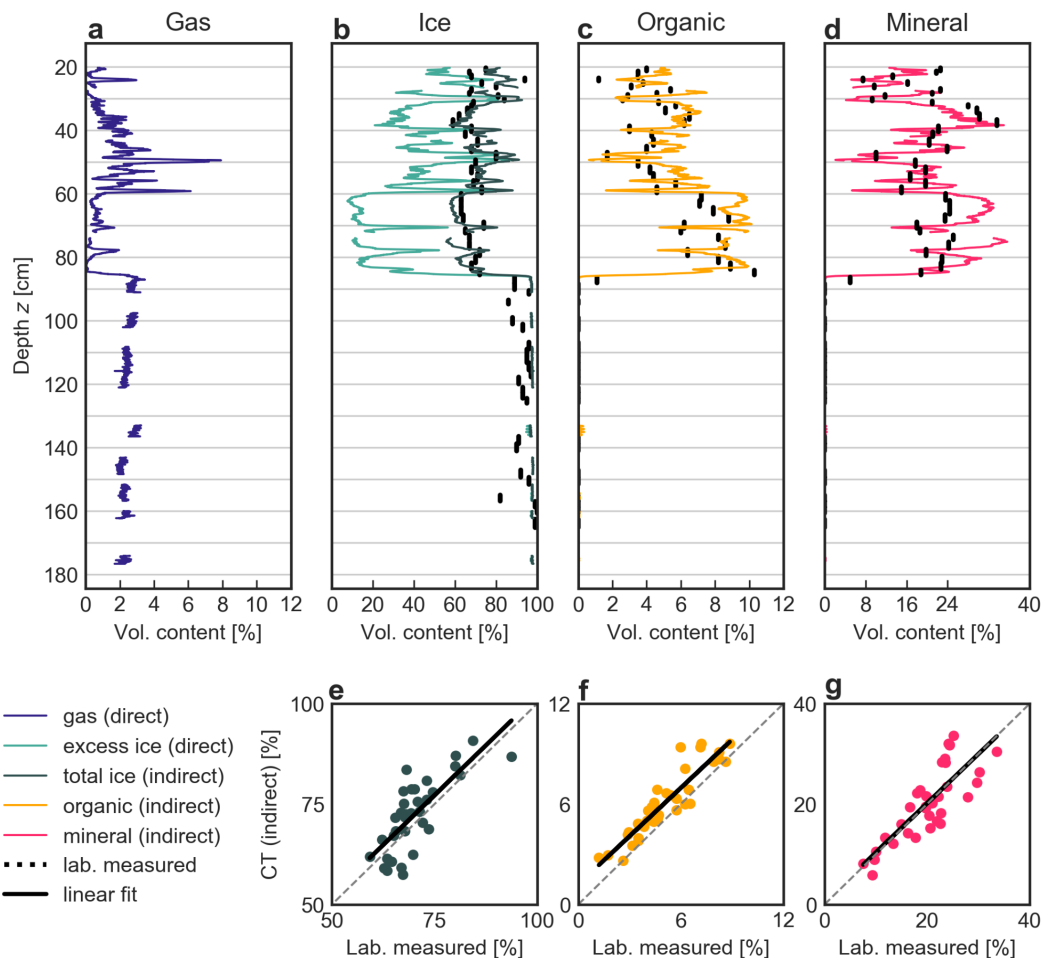


Figure 2. Vertical profiles of volumetric gas (a), ice (b), organic (c), and mineral (d) contents of the core. Gas and excess ice were derived directly from the CT images, while pore ice, organic, and mineral contents were derived indirectly using estimates of the composition of the sediment phases obtained from a linear regression against laboratory measurements. The lower panels (e,f,g) show the agreement between the CT-derived and the laboratory-measured contents. Note the different ranges of the horizontal axes for the different constituents.

since gas contents well above 1% were found in the upper (excess ice-rich) part of the core, the lower (pure excess ice) part, and also at the positions of ice lenses throughout sedimentary part of the core. In deviation from this pattern, gas contents were relatively low in the part around 30cm depth despite the presence of an ice lenses (Fig. 2 a,b). We hypothesize that partial melting of the excess ice in the uppermost part, e.g. in particularly warm and wet thawing seasons, could have destroyed gas inclusions, causing the absence of significant amounts of gas just below the active layer. Vice versa, this suggests that the excess ice layers in depths below 35cm preserved gas inclusions and could be present since the ice formation. In the lower part



of the core that consists of almost pure excess ice, gas contents were found to be almost constant at a level of about 2 to 3%. As gas contents cannot be determined directly in the laboratory, we could not compare the CT-derived profile to independent estimates.

155 **Excess ice contents** were found to be > 20% in the upper part and even exceed 30% in the section between 40 cm and 60 cm depth. Furthermore, the vertical profiles allowed us to identify ice lenses at approximate depths of 24 cm, 30 cm, 40 cm, 48 cm, 50 cm, 57 cm, 59 cm, 70 cm, and 78 cm as these are associated with distinct peaks in the excess ice contents exceeding 50 to 60%. In the lower part (> 85 cm depth) the core is composed of > 97% of excess ice with the remaining volume being filled with gas inclusions, as we found no significant sediment contents in the CT images. In the lower part as well as at the locations of ice lenses, the CT-derived excess ice contents agree well with the total ice contents determined from the lab samples (Fig. 2 b), with typical deviations of about 10% and maximum deviations of up to about 20%. In sediment-rich sections of the core (e.g. between 60 cm and 70 cm depth), the total ice contents measured in the laboratory were substantially higher than the excess ice contents derived directly from the CT. This can be explained by the presence of pore ice contained in the sediment phases A and B, which was included in the lab estimates, but could not be distinguished from the sediment matrix in the CT images.

3.3 Indirect estimation of pore ice, organic, and mineral contents

The vertical profiles of volumetric pore ice, organic, and mineral contents were calculated using Eq. (5) with the parameter values $\hat{\gamma}_{A/B,m/o/pi}$ as determined by the linear regression (Table 1). The best-fitting parameters for sedimentary phase A suggest an organic-rich ($\gamma_{A,o} = 0.14$) phase with a high porosity ($\gamma_{A,pi} = 0.68$). For phase B in turn, the composition parameters are indicative of a mineral phase ($\gamma_{B,m} = 0.49$) with a lower porosity ($\gamma_{B,pi} = 0.43$). We interpret phase A to correspond to peat inclusions in the sediment while phase B corresponds to a silty mineral matrix. We noticed that while the two sedimentary phases occur more spatially separated in the upper part of the core (see Fig. 1 e,f), they appear well-mixed in the middle part that is characterized by little excess ice (Fig. 1 g). This difference could be linked to higher degrees of cryoturbation and other mixing processes which the peat in the middle part of the core has undergone in the past.

170 The resulting vertical profile of the total ice content ($\theta_i(z) = \theta_{ei}(z) + \theta_{pi}(z)$; Fig. 2 b) shows a much-improved agreement with the ice contents determined from the lab samples ($R^2 = 0.59$), compared to directly determined excess ice profiles. The largest deviations were found at the locations of ice lenses, suggesting that these are not resolved by the coarse sample resolution of about 2 to 3 cm. In the sedimentary part of the core, the ice contents from the lab overall showed a low variability, ranging mostly between 60% and 70%. In contrast the CT-derived total ice content profile resolved details much better, and, for example, allowed the identification of the position of ice lenses. In addition, the CT-derived profiles allowed a robust distinction between pore and excess ice which is not possible with the standard laboratory procedure.

185 We found similarly good agreement between the CT-derived profiles and the laboratory-measured volumetric organic ($R^2 = 0.84$; Fig. 2 c) and mineral ($R^2 = 0.65$; Fig. 2 d) contents (Table 1). Despite the fact, that the laboratory measurement were used to derive the mineral and organic contents from the CT images, the good agreement provides credibility to the resulting high-resolution profiles which provide a much more detailed picture of the composition of the core. We note that while the



Table 1. Upper part: Composition of the sediment phases A and B derived through a linear regression against laboratory measurements (see Eqs. (4) and (5); given ranges are the standard errors of the regression).

Lower part: Evaluation metrics of the agreement between CT-derived and lab-measured volumetric organic, mineral and total ice contents (RMSE: root-mean-squared error; bias: mean difference CT-lab; slope and intercept of a straight line fit (ranges are standard errors); R^2 : coefficient of determination).

Sediment composition	pore ice		organic		mineral	
Phase A	$\gamma_{A,pi}$	0.68 ± 0.08	$\gamma_{A,o}$	0.14 ± 0.06	$\gamma_{A,m}$	0.18 ± 0.06
Phase B	$\gamma_{B,pi}$	0.43 ± 0.06	$\gamma_{B,o}$	0.07 ± 0.05	$\gamma_{B,m}$	0.49 ± 0.05
Evaluation metrics	total ice		organic		mineral	
RMSE [%]		6.13		1.30		4.27
bias [%]		2.27		1.00		0.15
slope [-]		0.99 ± 0.15		0.96 ± 0.08		0.98 ± 0.13
intercept [%]		2.7 ± 10.3		1.2 ± 0.5		0.5 ± 2.7
R^2 [-]		0.59		0.84		0.66

190 correspondence between CT profile and laboratory data is particularly good in the upper part of the core (< 60 cm), the relative deviations were slightly higher in the middle part. An additional, separate regression as described in Section 2.4 but restricted to the data available for the middle part of the core, could further improve the agreement between CT-derived and lab values further. However, such an approach would violate the assumption that the two sediment phases identified from the CT images are the same for the entire core.

4 Discussion and outlook

We successfully applied high-resolution CT as a non-destructive method to obtain the composition of a permafrost core. Compared to previous studies (Calmels and Allard, 2004), we report the highest spatial resolution in three dimensions of a permafrost core of $\Delta x = 50 \mu\text{m}$. From the CT images we identified four different material classes: gas, excess ice and two mixed sediment phases. Gas and excess ice were clearly distinguishable, confirming results of previous studies (Calmels and Allard, 2004, 2008; Calmels et al., 2012). Despite the high spatial resolution of the CT images, a robust distinction of the pore space (filled with pore ice), and the sediment matrix of the two mixed phases was not possible. One constraint to identify pores is given by the detection limit of 2-3 times the voxel size (Vogel et al., 2010; Withers et al., 2021). Therefore, in this study only gas pores, cracks and particles $> 100 \mu\text{m}$ were determined. A higher level of detail could only be achieved by smaller field of views and therefore at the expense of representativity. Another issue is the image noise. Higher acquisition times could in theory improve the image quality, but are problematic for frozen samples, as they could imply (partial) melting of the sample leading to changes in the material properties and potentially moving of the sample. Hence, the composition of the two sediment



phases could only be determined through an additional statistical regression against measurements obtained through destructive
205 laboratory analysis of the core. This indirect analysis revealed that the two sediment phases have distinct compositions in terms
of their volumetric pore ice, organic, and mineral contents, as well as different porosities, suggesting one phase to correspond
to organic-rich peat, and the other to be the silty mineral matrix. Overall, ground ice is the dominating constituent of the
studied permafrost core and it appears in different forms: excess ice in form of ice lenses, lenticular ice, and massive wedge
ice with minor gas inclusions; pore ice with volumetric fractions of about 43 to 68% in the two sediment phases. In agreement
210 with previous studies (Calmels and Allard, 2004), volumetric gas contents were small, with typical values of about 2% and
maximum values of up to 8%. Volumetric organic matter contents ranged between 2 and 10% in the sedimentary part of the
core, and showed a tendency to increase with depth.

Though manual thresholding resulted in robust segmentation results which were validated against visual inspection and
independent laboratory results, it is prone to some degree of subjectivity. Selecting the most applicable threshold is difficult
215 because the resolution of the CT will almost always be insufficient to resolve the phase or object of interest. For example,
the pore ice within the mineral matrix is often smaller than the spatial resolution of the CT. The resulting gray value of a
voxel is then a mixture of low-density ice and high-density minerals and may straddle around the threshold depending on the
exact proportions within such a partial volume voxel. In the future, the segmentation could be simplified by choosing a more
appropriate grayscale normalization than the percentile method. Homogeneous reference materials could be used to standardize
220 the gray values of all CT images prior to segmentation (Koestel, 2018). In permafrost soil, the histogram peaks of gas and ice
could be used. If these are not abundant enough to evoke distinct peaks, then rods of different material density (e.g. plastic
and aluminum) could be attached along the entire ice core so that they are present in all image segments to be identified as
reference materials. Segmentation of such normalized CT images by unsupervised classification (e.g., *k*-means clustering) can
be hampered by the fact that the number of material classes differs among individual scans (Schlüter et al., 2014). Therefore,
225 supervised, machine learning-based image segmentation is recommended in which a classifier is trained by drawing a few test
times for each materials class in small, but representative sub-volumes and then applied to all CT scans at once. State-of-the-art
machine-learning tool-kits allow to use high-level image features like gradient and texture at several length scales in addition
to normal grayscale information (Berg et al., 2019). In this way, material classes with with overlapping grayscale ranges could
be separated more accurately.

230 Our results introduce new perspectives on physical properties of permafrost and the processes shaping its microstructure.
For example, the full potential of 3D microstructure analysis is harnessed when morphological properties of individual material
classes are analyzed since structure and geometry control soil processes and properties. This could include, for example, the
aperture and spatial density of ice cracks in the sediment layer, the size, shape and density of gas entrapment in the excess ice
layers and identification of organic and mineral clusters. Using these information would allow improved estimates of physical
235 properties like the thermal conductivity or biochemical transport coefficients which depend on the constituents as well as their
spatial arrangement. Through additional analysis and combination with other measurements (e.g., age of material, grain size
distribution, etc.) physical processes such as sediment and ice accumulation rate, cryoturbation, bubble microstructure (Opel
et al., 2018) and pore resolution processes (Rooney et al., 2022) could be further studied with CT in the future. In summary,



our work is an important step towards establishing microstructure CT imaging as a technique for (i) estimating the physical
240 properties of permafrost ground and (ii) studying periglacial processes, allowing insights going far beyond classical destructive
laboratory analyses.

Code and data availability. The volumetric composition of the samples processed in the laboratory, the CT-derived composition at the same
coarse resolution, and the volumetric composition at the high spatial resolution of the CT are available from <https://doi.org/10.5281/zenodo.6397474>. This repository also contains the python script used for the least squares regression analysis.

245 *Video supplement.* Animated 3D-visualizations of a part of the segmented core images are provided at https://www.youtube.com/playlist?list=PLnngXB12Nji-oNXZkS8rAIwQrZQQvc2_X.

Author contributions. J.N. designed the study, was involved in the core drilling and CT image analysis, and led the manuscript preparation.
D.G. did the CT image analysis, assisted with the laboratory measurements, and created figures and visualizations. S.S. was involved in the
CT scanning and image analysis. J.M.K. led the CT scanning. G.G. advised on the methodology. J.B. initiated and supervised the study, and
250 was involved in the core drilling, CT scanning, and the laboratory analysis. All authors interpreted the results and contributed to the text of
the manuscript.

Competing interests. The authors declare that they have no competing interests.

Acknowledgements. The authors acknowledge assistance from the expedition, technical, and laboratory personnel at AWI Potsdam, es-
pecially Niko Bornemann and Bill Cable, and at UFZ Halle. This work was supported by a BMBF grant (project PermaRisk, grant no.
255 01LN1709A), and a grant of the Research Council of Norway (project PERMANOR, grant no. 255331). This work was supported by
funding from the Helmholtz Association in the framework of MOSES (Modular Observation Solutions for Earth Systems).



References

- Adams, W. A.: The Effect of Organic Matter on the Bulk and True Densities of Some Uncultivated Podzolic Soils, *Journal of Soil Science*, 24, 10–17, <https://doi.org/10.1111/j.1365-2389.1973.tb00737.x>, 1973.
- 260 Berg, S., Kutra, D., Kroeger, T., Straehle, C. N., Kausler, B. X., Haubold, C., Schiegg, M., Ales, J., Beier, T., Rudy, M., Eren, K., Cervantes, J. I., Xu, B., Beuttenmueller, F., Wolny, A., Zhang, C., Koethe, U., Hamprecht, F. A., and Kreshuk, A.: ilastik: interactive machine learning for (bio)image analysis, *Nature Methods*, 16, 1226–1232, <https://doi.org/10.1038/s41592-019-0582-9>, 2019.
- Calmels, F. and Allard, M.: Ice segregation and gas distribution in permafrost using tomodensitometric analysis, *Permafrost and Periglacial Processes*, 15, 367–378, <https://doi.org/10.1002/ppp.508>, 2004.
- 265 Calmels, F. and Allard, M.: Segregated ice structures in various heaved permafrost landforms through CT Scan, *Earth Surface Processes and Landforms*, 33, 209–225, <https://doi.org/10.1002/esp.1538>, 2008.
- Calmels, F., Allard, M., and Delisle, G.: Development and decay of a lithalsa in Northern Québec: A geomorphological history, *Geomorphology*, 97, 287–299, <https://doi.org/10.1016/j.geomorph.2007.08.013>, 2008.
- Calmels, F., Froese, D. G., and Clavano, W. R.: Cryostratigraphic record of permafrost degradation and recovery following historic
270 (1898–1992) surface disturbances in the Klondike region, central Yukon Territory, *Canadian Journal of Earth Sciences*, 49, 938–952, <https://doi.org/10.1139/e2012-023>, 2012.
- Cnudde, V. and Boone, M. N.: High-resolution X-ray computed tomography in geosciences: A review of the current technology and applications, *Earth-Science Reviews*, 123, 1–17, <https://doi.org/10.1016/j.earscirev.2013.04.003>, 2013.
- Kanevskiy, M., Shur, Y., Fortier, D., Jorgenson, M. T., and Stephani, E.: Cryostratigraphy of late Pleistocene syngenetic permafrost (yedoma)
275 in northern Alaska, Itkillik River exposure, *Quaternary Research*, 75, 584–596, <https://doi.org/10.1016/j.yqres.2010.12.003>, 2011.
- Koestel, J.: SoilJ: An ImageJ Plugin for the Semiautomatic Processing of Three-Dimensional X-ray Images of Soils, *Vadose Zone Journal*, 17, 170 062, <https://doi.org/10.2136/vzj2017.03.0062>, 2018.
- Kokelj, S. V. and Jorgenson, M. T.: Advances in Thermokarst Research, *Permafrost and Periglacial Processes*, 24, 108–119, <https://doi.org/10.1002/ppp.1779>, 2013.
- 280 Lapalme, C. M., Lacelle, D., Pollard, W., Fortier, D., Davila, A., and McKay, C. P.: Cryostratigraphy and the Sublimation Unconformity in Permafrost from an Ultraxerous Environment, University Valley, McMurdo Dry Valleys of Antarctica, *Permafrost and Periglacial Processes*, 28, 649–662, <https://doi.org/10.1002/ppp.1948>, 2017.
- Nitzbon, J., Westermann, S., Langer, M., Martin, L. C. P., Strauss, J., Laboor, S., and Boike, J.: Fast response of cold ice-rich permafrost in northeast Siberia to a warming climate, *Nature Communications*, 11, 2201, <https://doi.org/10.1038/s41467-020-15725-8>, 2020.
- 285 Oggier, M. and Eicken, H.: Seasonal evolution of granular and columnar sea ice pore microstructure and pore network connectivity, *Journal of Glaciology*, pp. 1–16, <https://doi.org/10.1017/jog.2022.1>, 2022.
- Opel, T., Meyer, H., Wetterich, S., Laepple, T., Dereviagin, A., and Murton, J.: Ice wedges as archives of winter paleoclimate: A review, *Permafrost and Periglacial Processes*, 29, 199–209, <https://doi.org/10.1002/ppp.1980>, 2018.
- Pribyl, D. W.: A critical review of the conventional SOC to SOM conversion factor, *Geoderma*, 156, 75–83, <https://doi.org/10.1016/j.geoderma.2010.02.003>, 2010.
- 290 Romanenko, K. A., Abrosimov, K. N., Kurchatova, A. N., and Rogov, V. V.: The experience of applying X-ray computer tomography to the study of microstructure of frozen ground and soils., *Earth's Cryosphere*, 21, [https://doi.org/10.21782/EC2541-9994-2017-4\(63-68\)](https://doi.org/10.21782/EC2541-9994-2017-4(63-68)), 2017.



- Rooney, E. C., Bailey, V. L., Patel, K. F., Dragila, M., Battu, A. K., Buchko, A. C., Gallo, A. C., Hatten, J., Possinger, A. R., Qafoku, O.,
Reno, L. R., SanClements, M., Varga, T., and Lybrand, R. A.: Soil pore network response to freeze-thaw cycles in permafrost aggregates,
295 *Geoderma*, 411, 115–124, <https://doi.org/10.1016/j.geoderma.2021.115674>, 2022.
- Schindelin, J., Arganda-Carreras, I., Frise, E., Kaynig, V., Longair, M., Pietzsch, T., Preibisch, S., Rueden, C., Saalfeld, S., Schmid, B.,
Tinevez, J.-Y., White, D. J., Hartenstein, V., Eliceiri, K., Tomancak, P., and Cardona, A.: Fiji: an open-source platform for biological-
image analysis, *Nature Methods*, 9, 676–682, <https://doi.org/10.1038/nmeth.2019>, 2012.
- Schirrmeister, L., Grosse, G., Wetterich, S., Overduin, P. P., Strauss, J., Schuur, E. A. G., and Hubberten, H.-W.: Fossil organic mat-
300 ter characteristics in permafrost deposits of the northeast Siberian Arctic, *Journal of Geophysical Research: Biogeosciences*, 116,
<https://doi.org/10.1029/2011JG001647>, 2011.
- Schlüter, S., Sheppard, A., Brown, K., and Wildenschild, D.: Image processing of multiphase images obtained via X-ray microtomography:
A review, *Water Resources Research*, 50, 3615–3639, <https://doi.org/10.1002/2014WR015256>, 2014.
- Schneider von Deimling, T., Lee, H., Ingeman-Nielsen, T., Westermann, S., Romanovsky, V., Lamoureux, S., Walker, D. A., Chadburn, S.,
305 Trochim, E., Cai, L., Nitzbon, J., Jacobi, S., and Langer, M.: Consequences of permafrost degradation for Arctic infrastructure – bridging
the model gap between regional and engineering scales, *The Cryosphere*, 15, 2451–2471, <https://doi.org/10.5194/tc-15-2451-2021>, 2021.
- Schuur, E. A. G., McGuire, A. D., Schädel, C., Grosse, G., Harden, J. W., Hayes, D. J., Hugelius, G., Koven, C. D., Kuhry, P., Lawrence,
D. M., Natali, S. M., Olefeldt, D., Romanovsky, V. E., Schaefer, K., Turetsky, M. R., Treat, C. C., and Vonk, J. E.: Climate change and the
permafrost carbon feedback, *Nature*, 520, 171–179, <https://doi.org/10.1038/nature14338>, 2015.
- 310 Strauss, J., Schirrmeister, L., Grosse, G., Fortier, D., Hugelius, G., Knoblauch, C., Romanovsky, V., Schädel, C., Schneider von Deimling,
T., Schuur, E. A. G., Shmelev, D., Ulrich, M., and Veremeeva, A.: Deep Yedoma permafrost: A synthesis of depositional characteristics
and carbon vulnerability, *Earth-Science Reviews*, 172, 75–86, <https://doi.org/10.1016/j.earscirev.2017.07.007>, 2017.
- Torrance, J. K., Elliot, T., Martin, R., and Heck, R. J.: X-ray computed tomography of frozen soil, *Cold Regions Science and Technology*,
53, 75–82, <https://doi.org/10.1016/j.coldregions.2007.04.010>, 2008.
- 315 Vogel, H. J., Weller, U., and Schlüter, S.: Quantification of soil structure based on Minkowski functions, *Computers & Geosciences*, 36,
1236–1245, <https://doi.org/10.1016/j.cageo.2010.03.007>, 2010.
- Withers, P. J., Bouman, C., Carmignato, S., Cnudde, V., Grimaldi, D., Hagen, C. K., Maire, E., Manley, M., Du Plessis, A., and Stock, S. R.:
X-ray computed tomography, *Nature Reviews Methods Primers*, 1, 1–21, <https://doi.org/10.1038/s43586-021-00015-4>, 2021.